

Paper 3

3

Simulating the laminar von Kármán flow in Nek5000

By **E. Appelquist**^{1,2} and **P. Schlatter**^{1,2}

¹Linné FLOW Centre, KTH Mechanics, SE-100 44 Stockholm, Sweden

²Swedish e-Science Research Centre (SeRC)

Technical report, 2014

The laminar incompressible boundary layer over a rotating disk, also called the von Kármán flow, is investigated. The goal is to set up a direct numerical simulation (DNS) environment for further use to investigate the transition from laminar to turbulent flow for this boundary layer. For this the spectral-element code Nek5000 is used. A set of ODE-equations are first derived from the incompressible cylindrical Navier–Stokes equations, which are solved for the exact von Kármán solution. Further, Nek5000 is prepared to solve for the same laminar solution. Comparing the two solutions give a quantification of the accuracy of the DNS solver Nek5000. Different scalings of the equations are investigated, together with quantifications of how good the different available boundary conditions are, also investigating different reference frames and grid dependency of the solution. The general conclusion is that the von Kármán flow is possible to simulate in Nek5000. The method was robust when it came to using different scalings, reference frames and resolutions.

1. Introduction

This report discuss the laminar flow over an infinite rotating disk, also called the von Kármán flow. This is a three-dimensional (3D) boundary layer, for which, the similarity solution to the Navier–Stokes equations in cylindrical coordinates can be described by three 1D profiles, see figure 1. This solution was first derived by von Kármán (1921) and research on this flow has been ongoing ever since.

Since an exact similarity solution exist, this flow has been analysed for its linear stability properties. One experimental observation which is specific to the rotating-disk boundary layer is the seemingly sharp edge that separates laminar from turbulent flow. Conversely, in flat-plate boundary layers (be it two or three-dimensional) transition is much more irregular, very much in agreement with the idea of a convective instability. Following this observation, Lingwood (1995) showed that there is a local absolute instability present above

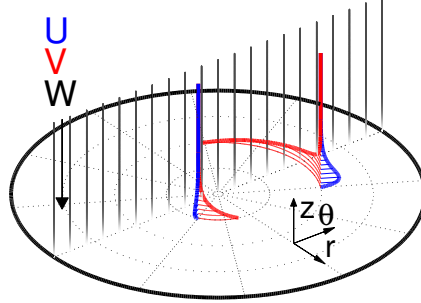


FIGURE 1. The laminar velocity profiles of the flow over a rotating disk. U is the radial velocity component, V is the azimuthal velocity component and the vertical greyscale lines indicate the profile for W (white is zero velocity).

a nondimensional radius ($r = r^*/L^*$ where $L^* = \sqrt{\nu/\Omega^*}$, ν is the kinematic viscosity and Ω^* is the rotation rate) of 510. This number is later updated in Lingwood (1997) from 510 to 507. This local absolute instability was later concluded *not* to be transferred to the global (non-parallel) case by *linear* direct numerical simulations (DNS) (Davies & Carpenter 2003). However, the global instability characteristics of the rotating-disk boundary layer are still the subject of ongoing research. An extension to the linear DNS work done by Davies & Carpenter (2003) is of interest to contribute to a better understanding of the linear stability characteristics, along with nonlinear DNS of the flow, which can serve as a direct comparison to the experimental work. DNS has some advantages over experiments and it is possible to play with parameters in a more elaborate way. In order to perform such simulations a stable numerical setup is needed that is sufficiently accurate. Furthermore, the code has to be numerically efficient since extensive computations will be needed to make the calculations. Once a setup and code has been chosen, the first test case is to obtain the laminar von Kármán flow described in this report. Herein, there will only be a description of the laminar flow in order to investigate the robustness of Nek5000. Mainly the purpose is to investigate numerical parameters such as the grid structure, boundary conditions and resolution.

The following section describes the solution of the von Kármán equations using numerical methods. The DNS code Nek5000 will be discussed in section 3. The scaling of the equations will be further discussed in section 4, followed by sections investigating the solution of Nek5000 by examining the different reference frames available (section 5), the dependency of the chosen boundary conditions (section 6) and the grid dependency of the solution (section 7). Section 8 will further discuss simulations when extending the domain to higher

Reynolds numbers. Some concluding remarks together with an outlook for further runs will be given in section 9.

2. Solving for the similarity solution using the shooting method

The equations governing the flow over the rotating disk are the incompressible Navier–Stokes and the continuity equation in cylindrical coordinates (r, θ, z) ,

$$\begin{aligned} \frac{\partial U^*}{\partial t^*} + \mathbf{U}^* \cdot \nabla U^* - \frac{V^{*2}}{r^*} - 2\Omega^* V^* - \Omega^{*2} r^* \\ = -\frac{1}{\rho} \frac{\partial P^*}{\partial r^*} + \nu \left(\nabla^2 U^* - \frac{U^*}{r^{*2}} - \frac{2}{r^{*2}} \frac{\partial V^*}{\partial \theta} \right) \end{aligned} \quad (1)$$

$$\begin{aligned} \frac{\partial V^*}{\partial t^*} + \mathbf{U}^* \cdot \nabla V^* + \frac{U^* V^*}{r^*} + 2\Omega^* U^* \\ = -\frac{1}{r^* \rho} \frac{\partial P^*}{\partial \theta} + \nu \left(\nabla^2 V^* + \frac{2}{r^{*2}} \frac{\partial U^*}{\partial \theta} - \frac{V^*}{r^{*2}} \right) \end{aligned} \quad (2)$$

$$\frac{\partial W^*}{\partial t^*} + \mathbf{U}^* \cdot \nabla W^* = -\frac{1}{\rho} \frac{\partial P^*}{\partial z} + \nu \nabla^2 W^* \quad (3)$$

$$\frac{\partial U^*}{\partial r^*} + \frac{U^*}{r^*} + \frac{1}{r^*} \frac{\partial V^*}{\partial \theta} + \frac{\partial W^*}{\partial z^*} = 0 \quad (4)$$

where U, V and W are the radial, azimuthal and wall-normal velocities and P is the pressure. ν is the kinematic viscosity, ρ is the density, Ω is the rotation rate and t is time. The star superscript means that the quantities are dimensional. Included are the centrifugal force and the Coriolis force, respectively, $-\Omega^* \mathbf{e}_z \times (\Omega^* \mathbf{e}_z \times r^* \mathbf{e}_r) = \Omega^{*2} r^* \mathbf{e}_r$ and $-2\Omega^* \mathbf{e}_z \times \mathbf{U}^* = 2\Omega^* V^* \mathbf{e}_r - 2\Omega^* U^* \mathbf{e}_\theta$, where $\mathbf{e}_r, \mathbf{e}_\theta$ and \mathbf{e}_z are the unit vectors in each direction.

The similarity variables are functions of z alone. For the global scale these are $U(z) = U^*/r^* \Omega^*$, $V(z) = V^*/r^* \Omega^*$, $W(z) = W^*/(\nu \Omega^*)^{1/2}$, $P(z) = P^*/\rho \nu \Omega^*$, $z = z^*/L^*$ and $r = r^*/L^*$ where $L^* = (\nu/\Omega^*)^{1/2}$. The nondimensional Reynolds number can be rewritten by using the similarity variables

$$R = \frac{r^* \Omega^* L^*}{\nu} = r^* \frac{1}{L^{*2}} L^* = \frac{r^*}{L^*} = r, \quad (5)$$

that is, the Reynolds number is equal to the nondimensional radius. Using these global-scale similarity variables in the governing equations, (1)–(4), and assuming that the base flow is independent of θ and steady in time the following ordinary nonlinear differential equations are obtained

$$2U + W' = 0 \quad (6)$$

$$U^2 - (V + 1)^2 + U'W - U'' = 0 \quad (7)$$

$$2U(V + 1) + V'W - V'' = 0 \quad (8)$$

$$P' + WW' - W'' = 0 \quad (9)$$

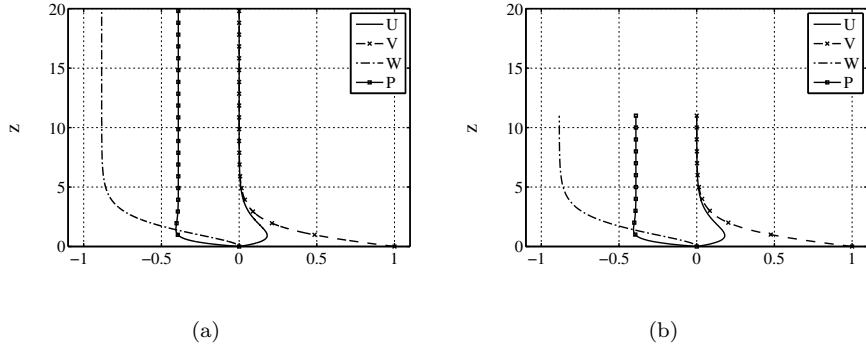


FIGURE 2. Similarity solution for the flow over a rotating disk. The solution is shown in the laboratory frame of reference. Results obtained from (a) the ODE solution and (b) DNS performed with Nek5000.

where the prime denotes differentiation with respect to z . The above equations were solved by using the Runge–Kutta fourth order (RK4) method with a Newton–Raphson searching method (from now on referred to as the ODE solution). The boundary conditions used are: no slip at the wall, $U(0) = 0$ and $V(0) = 0$; $W(0) = 0$ due to the impermeability of the disk; and a far field boundary condition implying no viscous effects far from the wall giving $U(z \rightarrow \infty) = 0$ and $V(z \rightarrow \infty) = -1$. Note that the equations are solved in the rotating frame of reference where the rotation was set to $\Omega = 1$. The z -domain spanned from $0 - 20$ containing approximately 10000 gridpoints with the possibility either to be equidistant or adapted to a spectral-element mesh. Further details on the solution procedure can be found in paper 4 in this thesis, Appelquist & Imayama (2014). The resulting profiles are shown in both figure 1 and in figure 2. Figure 1 illustrates the global profiles in the laboratory frame of reference, and it particularly shows the linear increase of the U and V components with radius. Also, it shows that the boundary layer height is constant with radius as seen from the W profile (greyscale). Figure 2(a) shows the profiles normalized to $r = 1$, also this in the laboratory frame of reference. Figure 2(b), shows the outcome from the DNS in Nek5000 discussed later. The profiles obtained from the ODE solution are used to set both initial and boundary conditions when needed in Nek5000.

This von Kármán flow is driven by the disk itself and is one of the simplest 3D boundary layers not least because the similarity profiles only depend on the height (z). Similarities can be found to the boundary-layer flow over a swept wing, since both flows contain an inflectional laminar velocity component, meaning that they are susceptible to certain instabilities triggering transition to turbulent flow. Although for the rotating disk, many of the parameters are

eliminated compared to the swept wing, such as the sweep angle and pressure gradient, simplifying the experimental configuration compared with the wing case.

3. Nek5000

The simulations were performed with the massively parallel spectral-element code Nek5000 (Fischer *et al.* 2012). Nek5000 is a Legendre polynomial based spectral-element method code which solves the incompressible Navier–Stokes equations. The temporal discretization scheme used is based upon operator splitting, where the nonlinear convective terms are treated explicitly via a projection scheme, and the viscous and divergence operators are treated implicitly (Deville *et al.* 2002). The scheme is based on the backward differential formula (BDF) where, for the nonlinear terms it is extrapolating (EXT). Equation (15) in Karniadakis *et al.* (1991) corresponds to the operative scheme BDFk/EXTk, where in Nek5000 orders of $k=1-3$ are possible. There is also a possibility to turn off the nonlinear terms and only run the code in a linear fashion.

3.1. Meshing

The spectral elements within the code are flexible and can be used to build complex geometries. The geometries used for the rotating-disk case are seen in figures 3(a) and (b). They are further extended in the third wall-normal direction, where the elements are stretched by a factor $s = 1.15$ according to

$$z_n = \sum_{i=0}^{i=n} \Delta z s^{i-2} \quad (10)$$

with highest resolution close to the disk surface. Here z_n is the coordinate at position n above the wall and $\Delta z = 0.2$ is the spectral element closest to the wall, followed by 16 elements to a height of $z = 11.1$. An example of the elements distribution after this stretching is seen within figure 4 as lines parallel to the x -axis. Using 16 elements in the vertical direction gives a mesh of 3072 elements when using the mesh of the whole disk, figure 3(b), containing 192 elements at each level. For all the simulations presented in this report, 9 collocation points are introduced for each element, where the solution is approximated using 8th order polynomials. This corresponds to a mesh containing elements that themselves are divided into 8 small elements in each direction, as seen in figure 3(a) and (b). To obtain spectral accuracy these grid points are distributed according to Gauss-Lobatto-Legendre (GLL) quadrature points. The total number of grid points for mesh (b) thus becomes $3072 \cdot 8 \cdot 8 \cdot 8 = 1,572,864$.

The already calculated ODE solution of the von Kármán similarity solution is, as already mentioned, used to set the initial and Dirichlet boundary conditions. This solution is provided in double precision on the predicted GLL

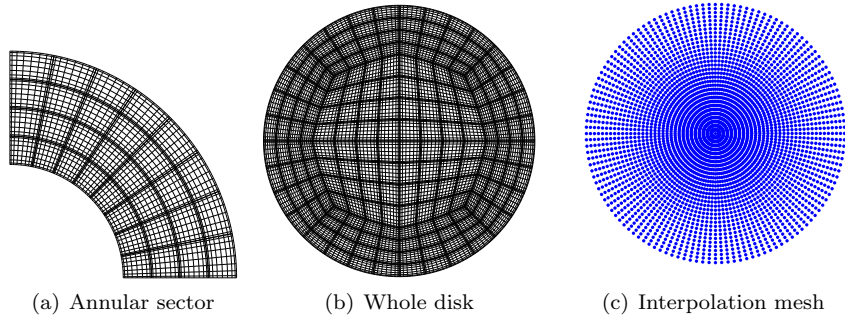


FIGURE 3. 2D visualizations of the meshes used in the Nek5000 simulation. (a) and (b) show the computational meshes and (c) shows the interpolation mesh with further information in table 1.

	interval	Δ	n
r	0–100	3.125	33
θ	$\pi/64$ – 2π	$\pi/64$	128
z	0–11	0.1	111

TABLE 1. Table of points in connection to the interpolation grid of figure 3(c).

points of the Nek5000 mesh. Since the similarity solution depend on z , before assigning the solution to the gridpoints in Nek5000 these are checked to correspond to the exact GLL points of the ODE solution. The similarity solution is then first assigned to the points in the z -direction, followed by a scaling of the profile in r from recognizing the x and y positions (Cartesian grid) of the specific grid point.

3.2. Interpolation

Within Nek5000 there is a possibility to interpolate the data with spectral accuracy. This is done to a new cylindrical grid in order to further post-process the data in Matlab easily. When doing so, there is less data to handle in the post-processing step and the data can be structured as desired making it easier to handle than the points given by the original GLL points. It is thus important that the interpolation routine works accurately. The interpolation grid corresponding to the mesh of the whole disk is seen in figure 3(c) and the gridpoints can be calculated based on the information given in table 1 where the radius is assumed to be 100 and the height of the domain 11. The interpolation points are here chosen so that the outer part of the grid has 4

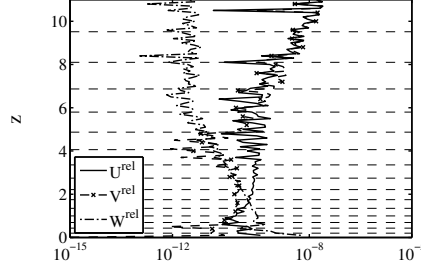


FIGURE 4. Relative interpolation error (see equation (11) for $t = 0$) as a function of height of the velocity profiles at a position of $r = 50$ and $\theta = \pi/4$.

points per element in the radial and azimuthal direction. In the inner part of the grid, the number of points per element becomes larger due to the polar structure of the interpolation grid.

The interpolation error for the velocity field can be estimated by setting the similarity solution as an initial condition in Nek5000, and then outputting this same field when interpolated to the mesh of figure 3(c). The amplitude of the relative error is seen in figure 4 as a function of height (z), at a position $r = 50$ and $\theta = \pi/4$ when using the mesh in figure 3(b). The relative error is calculated by taking the interpolated Nek5000 solution, subtracting the ODE solution, and then dividing by the ODE solution,

$$\mathbf{U}^{rel} = \left| \frac{\mathbf{U}^t - \mathbf{U}_{ODE}}{\mathbf{U}_{ODE}} \right|, \quad (11)$$

where the time $t = 0$. The values are seen to lie within the range $10^{-12} - 10^{-8}$. The U and V profiles have an increasing error with height whereas the W error decreases with height. This is since the U and V profiles approach zero as $z \rightarrow 20$ for the ODE solution and the uncertainty of the relative error becomes larger. This is not due to the decrease in resolution when moving further away from the wall. At certain positions the interpolation routine was less accurate. This will be brought under closer attention when discussing the grid dependency of the solution in section 7.

To evaluate the interpolation routine for the pressure, Nek5000 had to first calculate the pressure before it could be compared. This relative error is seen in figure 6(a) together with the relative errors for the velocity components after one rotation. The values are taken from a converged run called sc3. These errors will be discussed later however the figure shows that the interpolation routine also gives good results for the pressure where the procedure is initially different compared with the velocities. For the pressure, there is an extra mapping step involved since there is a difference between the velocity grid and

the pressure grid (P_N - P_{N-2} method). The velocity field is calculated on the mesh seen in figure 3(b), that is on the GLL points, whereas the pressure is calculated on a grid only containing the Gauss-Legendre (GL) points (the endpoints are not included). For the pressure the GL points are mapped to GLL points before interpolating. There is also a possibility to use the same gridpoints for the pressure as for the velocities (P_n - P_n method), meaning all values in the simulations are calculated on the GLL points. This gave results corresponding to the P_n - P_{n-2} method, both for the interpolation routine and in general for the simulations.

3.3. Setup

The first simulations of the von Kármán flow in Nek5000 presented in this report used Dirichlet boundary conditions on all boundaries. The Reynolds number at the edge of the disk was set to 100, and these first simulations were done using the nonlinear version of the code with time integration order $k=3$. Also a stabilizing filter with a weight of 5% for the last mode (highest wavenumber) was used. The von Kármán field can later be used as the baseflow for the linear version of the code although, in this report, everything is done nonlinearly.

Using $\Omega = 1$ creates a simple way of measuring time, since it is then always equal to the radians the disk has rotated through. For the laminar simulations using the mesh of the whole disk, figure 3(b), the time step was $\Delta t = \pi \cdot 10^{-3}$ and the number of time steps was $n = 2000$, leading to a total time of $T = \Delta t \cdot n = 2\pi$, corresponding to one rotation. During the single rotation of the disk simulation, data is stored 16 times, every 125th step. The Courant–Friedrichs–Lewy (CFL) condition for these first specific simulations was then 0.425 indicating the run should be stable since it is below 0.5.

4. Simulations in Nek5000 with different scaling

It is possible to use different scalings of the similarity solution in Nek5000. Three comparable simulations using the mesh of figure 3(b) have been made to both explain this scaling and make sure there is no difference between them when simulating the flow. The three runs are named sc1, sc2 and sc3, and they used the nondimensional lengthscales $L = L^*/(100L^*) = 1/100$, $L = 1/10$ and $L = 1/1$, respectively. When simulating Reynolds numbers up to 100, the edge of the disk corresponds to radius 1, 10 and 100 referring to each lengthscale. It is thus only the last case (sc3) that is equivalent to (5) where $R = r$. For the other cases $R = 100r$ (sc1) and $R = 10r$ (sc2). This is since r now is scaled according to the new lengthscales; $r = r^*/(xL^*)$ and thus $r^*/L^* = xr$ where x is 100 (sc1) or 10 (sc2). Within Nek5000 the Reynolds number is defined using nondimensional variables, $R = Lr\Omega/\nu$. A fixed computational Reynolds number is set according to $R_{model} = 1/\nu = R/(Lr\Omega)$ where $\Omega = 1$ in our simulations for simplicity (Ω is radians per nondimensional time unit). Using

the values at the edge to determine this R_{model} gives for sc1 $R_{model} = 100^2$ since for $R = 100$, $r = 1$. For sc2 $R_{model} = 10^2$ and for sc3 $R_{model} = 1$.

The results from the simulations with the three scalings are all shown in figure 2(b) since they all coincide with each other. 1D profiles are seen from 3D simulations. This is since the solution is averaged both in the azimuthal and radial direction however in the radial direction, both the U and V profile have to be rescaled by the local radius before averaging. The calculations for the profiles are

$$U_{1D}(z) = \frac{1}{2\pi} \frac{1}{(r_2 - r_1)} \int_{r_1}^{r_2} \int_0^{2\pi} \frac{U}{r} d\theta dr \quad (12)$$

$$V_{1D}(z) = \frac{1}{2\pi} \frac{1}{(r_2 - r_1)} \int_{r_1}^{r_2} \int_0^{2\pi} \frac{V}{r} d\theta dr \quad (13)$$

$$W_{1D}(z) = \frac{1}{2\pi} \frac{1}{(r_2 - r_1)} \int_{r_1}^{r_2} \int_0^{2\pi} W d\theta dr \quad (14)$$

$$P_{1D}(z) = \frac{1}{2\pi} \frac{1}{(r_2 - r_1)} \int_{r_1}^{r_2} \int_0^{2\pi} P d\theta dr. \quad (15)$$

The points at the radial boundary are not included since the boundary values are already set from the ODE solution. The terms r_1 and r_2 are thus precisely excluding the inner and outer boundaries of the domain in the radial direction. The obtained 1D solution is a good measure by which to compare the Nek5000 solution to the ODE solution of the von Kármán flow. The two solutions are seen in figure 2(a), the ODE solution, and (b), the Nek5000 solutions. The reference level of the pressure for the Nek5000 profiles were first shifted for a zero wall value.

Before comparing the individual runs to the ODE solution, the development in time is investigated to make sure the solution after one rotation is converged. The 1D profiles shown in figure 2(b) are used to determine the change of the model in time. This is done by taking the mean of the difference in time of the profiles,

$$\Delta \mathbf{U}_{1Dz} = \frac{1}{Z} \int_0^Z |\mathbf{U}_{1D}^{t+\Delta T} - \mathbf{U}_{1D}^t| dz \quad (16)$$

where $Z = 11.1$. The time difference is the time between two stored times; $\Delta T = 125 \cdot \pi \cdot 10^{-3}$. Figure 5 shows $\Delta \mathbf{U}_{1Dz}$ for the sc3 run. The pressure quantity (not shown) was of the order of 10^{-8} corresponding to the value of the divergence operator set in Nek5000. Again, there was no significant difference between the three runs and all values reach an approximately constant level for large times. Computing the relative error of U , V , W and P to the ODE solution as a function of height at the last time step using equation (11) where $t = T$ gives figure 6 for the sc3 run, which is comparable to figure 4 where $t = 0$. The errors were again of the same order for all runs (sc1, sc2 and sc3). Figure 6(a) shows the relative errors for just one r - θ position ($r = 50$ and $\theta = \pi/4$),

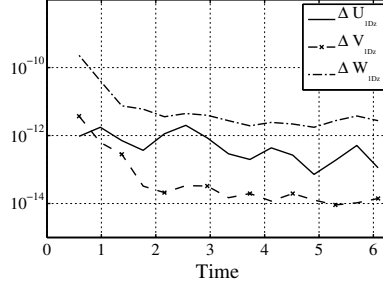


FIGURE 5. The y -axis show the difference of the values in time of the averaged 1D profiles for the sc3 run, see equation (16), and the time (t) is shown in radians.

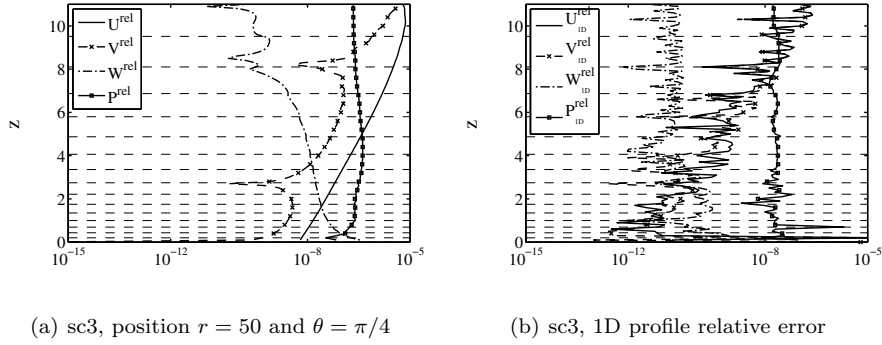


FIGURE 6. Relative error as a function of height (z) for the sc3 run after one rotation ($T = 2\pi$).

and (b) shows the relative errors of the 1D profiles (exchange \mathbf{U}^T to \mathbf{U}_{1D}^T in (11) to get \mathbf{U}_{1D}^{rel}). Within the figures, the vertical distribution of elements is also shown. Comparing figure 4 and figure 6(a) the error has become larger and smoother over time. There are thus additional errors entering the flow field possibly depending on the grid resolution or the domain height for example. In figure 6 it is also seen that the relative error of the pressure is larger than the relative errors of the velocity profiles.

A comparison of the time per time step was made to see if there is a difference in computational time for the different scalings used, seen in table 2. The number of cores used for these simulations was 10 and the runs were done locally on a 12 core computer. When comparing the time per time step, a significant difference between all the runs can be observed as shown in the table. The sc1 run was seen to be faster than sc2 which was faster than sc3. When

run	HELMHOLTZ	time/time step (sec.)
sc1	10^{-8}	3.73
sc2	10^{-9}	3.90
sc3	10^{-10}	4.48
rot_fr	10^{-10}	4.52

TABLE 2. Various runs for different scaling together with the HELMHOLTZ parameter value normalized to the scaling of the sc1 run. The rotating reference frame run (rot_fr) is in the same scaling as sc3 and thus comparable to this run.

taking a closer look at the runs, they had different iteration numbers for the velocity convergence in the Helmholtz solver. The parameter controlling this is called HELMHOLTZ in Nek5000. This number was set to be equal in all runs (10^{-8}) however it was concluded to be an absolute value meaning this affects the run differently depending on the scaling. When this parameter was decreased to 10^{-6} in sc3 (since the scaling differs by a factor 100), the result from sc1 was recovered. In table 2 the HELMHOLTZ parameter value with respect to sc1 is seen together with data how the time/time step is affected by it. Thus, when increasing the accuracy of the simulation, more iterations are needed for the Helmholtz solver and this increases the time per time step. However, this accuracy difference is not seen in the results when comparing *e.g.* figure 6 for the three simulations. This indicates that the dominating errors are not due to the convergence of the Helmholtz part, but to other aspects of the setup. The time per time step can thus be optimized by setting the HELMHOLTZ parameter as high as possible without affecting the results. There is one more run not discussed yet in the same table which will be discussed in the next section.

The results shown above indicate that the three scalings are equivalent. However, there is one advantage of sc3 and this is the fact that $R = r$. This scaling is found in all theoretical and experimental reports (*e.g.* Lingwood 1995; Imayama *et al.* 2012) and will thus be the natural choice. All further simulations are therefore made according to the sc3 scaling.

5. Simulations in the rotating reference frame

Simulating the rotating reference frame, forcing terms were added to the explicit scheme consisting of the Coriolis and the centrifugal force. The forcing terms added in the x and y direction are then, respectively, $2\Omega V + \Omega^2 x$ and $-2\Omega U + \Omega^2 y$.

The difference between the rotating reference frame and the laboratory reference frame is then the V profile where, respectively, $V = 0$ and $V = 1$, at the wall. In Nek5000, the rotating reference frame runs became identical to

	Nek5000 notation	formulation
Dirichlet	v	$\mathbf{u} = (u, v, w)$
Homogenous Neumann	O	$\mathbf{n} \cdot (\nu \nabla \mathbf{u} - p \mathbf{I}) = \mathbf{0}$
Boundary-layer condition	ON	$u = u, v = v, \partial W / \partial z = p / \nu$

TABLE 3. Table of boundary condition available in Nek5000. ON case is shown for a surface with the normal in the z -direction.

the laboratory frame ones when comparing development in time. The resulting relative errors were also in the same order as for the laboratory frame of reference.

A difference was seen in the time per time step shown in table 2. There is a slight increase for the rotating reference frame compared to the laboratory frame of sc3 possibly due to the extra forcing term included in the simulation for this case.

6. Simulations with various boundary conditions

So far, the simulations have been conducted with Dirichlet boundary conditions everywhere. These are denoted with v, consistent with the notation in Nek5000. As already mentioned, this boundary condition is defined by setting the velocities at the boundaries to predetermined values, here they consist of the values obtained from the ODE solution to the von Kármán equations. Since these boundary conditions already provide information about the solution, they are expected to be the most accurate ones. There are other available boundary conditions in Nek5000 and they are summarized in table 3. The homogenous Neumann boundary condition, denoted O in Nek5000 due to the outflow nature, is the stressfree condition and also the natural boundary condition for the spectral-element method. If r is the normal direction to the boundary O becomes $\nu \partial U / \partial r - p = 0$, $\partial V / \partial r = 0$ and $\partial W / \partial r = 0$ at the boundary. For the rotating-disk boundary layer this boundary condition does not concur with the similarity solution. The desired outflow condition in the radial direction is thus not the homogenous Neumann condition, but the corresponding condition with respect to a rotational system, that is $dU/dr = r$, $dV/dr = r$ and $dW/dr = 0$. The reason for this formulation is the global increase of U and V with radius, and the fact that the boundary layer height is constant. In order to formulate such conditions, a Neumann condition currently not available is needed however an investigation needs first to be done if such a condition would be stable in Nek5000.

There is one more boundary condition relevant to our flow case, the ON boundary condition. This is a mix of v and O first developed to suit the Blasius boundary layer, where the velocities in the plane at the top boundary were set

as v , whereas the velocity in the normal direction was set to O . In this sense the flow can escape at its own pace (*i.e.* it allows transpiration). In a similar way, for the rotating disk, the ON boundary condition can be used at the top of the domain to set both U and V , but leave W as $\partial W/\partial z = p/\nu$. This formulation of the ON condition can be found in table 3, and considering a constant pressure in the radial direction, the wall-normal velocity gradient is constant. In both the case of the Blasius boundary layer and for the rotating-disk boundary layer, this constant equals zero since Nek5000 then normalizes the pressure at this boundary, giving $\partial W/\partial z = 0$. The main difference between the two boundary layers is that the rotating-disk boundary layer has a negative W component meaning that the flow is not leaving but rather entering the domain. However, the desired boundary condition for the rotating-disk boundary layer on the top is actually $\lim_{z \rightarrow \infty} \partial W/\partial z = 0$, although, it is not possible to map the boundary to infinity and the domain has to be cut. For U and V there are then two options, either they are set to the ODE solution at the top (ON), or they are set to exactly zero at the top (ON_0).

Various runs elaborating the boundary conditions can be seen in figure 7, where the colour scale is in \log_{10} scale. All subplots show the amplitude of the relative error of the azimuthal mean values of W , obtained by Nek5000 compared to the ODE solution. This time, there is no averaging with radius to obtain the 1D profile discussed earlier. The axes seen are then showing the height z and the radial direction r . The reason why W is chosen is because the U and V profiles both approach zero as $z \rightarrow \infty$. Figure 7(a), (b) and (c) differ in the top boundary condition used. (a) use v on top, (b) use ON at the top where the U and V values are set to the von Kármán flow, which is different in (c), where ON_0 is used where U and V are set to zero, which is the limit when $z \rightarrow \infty$. Comparing the top boundary for the three runs, the v and ON are very similar containing the same order of the error. There is a large error in (c) where the error at the top boundary increases with the radius, which can be expected since the U and V increase linearly with radius and thus the difference to zero from the von Kármán profile does the same, also contaminating the W -component by continuity. Notice also the change of colour scale indicating much larger errors than the previous cases. It is interesting to see that this error is spread down through the whole domain. An additional comment that can be made for figure 7(a) and (b) is that the maximum error is following where the highest gradient of the similarity profiles are located.

Investigating the effect of different radial boundary condition, figure 7(b) and (e) are compared, having, respectively, v and O at the radial boundary. Once again, the colourscales are different in the two figures, and the O boundary experience a larger error throughout the whole domain. This is reasonable since O tries to set the derivatives in r to zero, however, this is only satisfied by one of the velocity components, W . U and V both increase linearly with r and

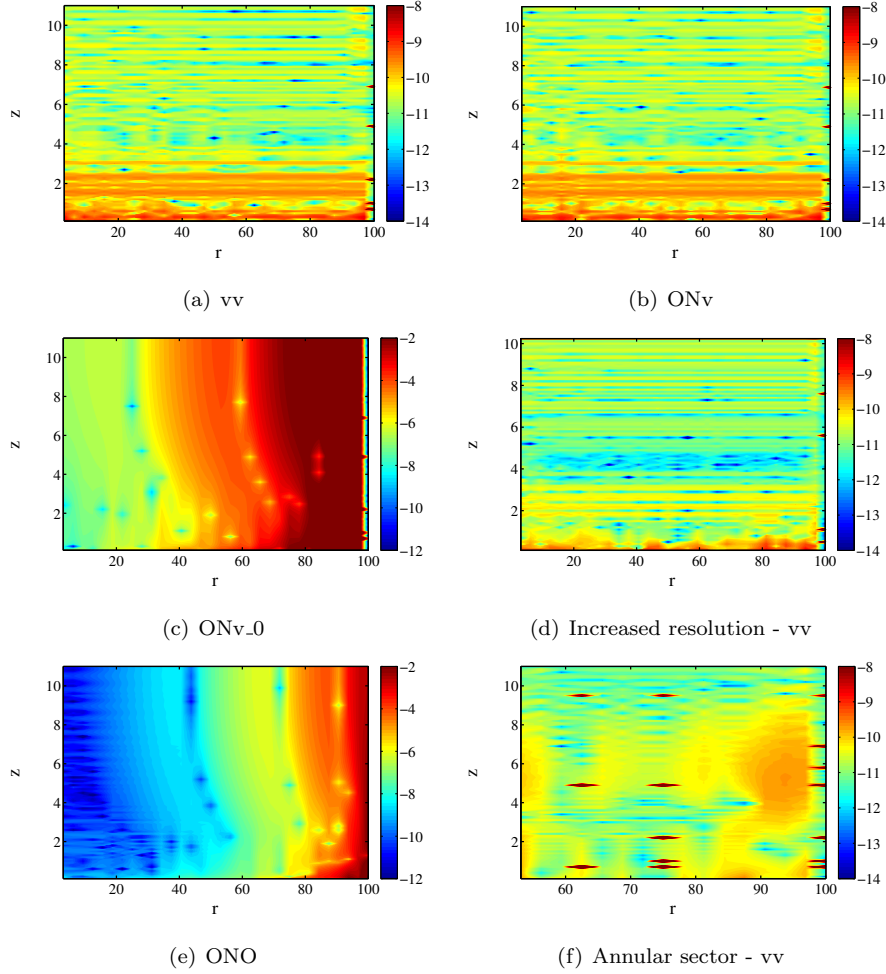


FIGURE 7. Relative error of W averaged in the azimuthal direction at the last time step. r and z is shown on the x and y axis, respectively, and the colour bar is shown in \log_{10} scale. The first letters denotes the top boundary condition and the last letter the radial boundary condition.

thus using a homogeneous Neumann condition for these will not satisfy our flow and the errors become large close to the boundary decreasing inwards. The preferred condition in the radial direction is thus v .

When simulating the annular sector there is one additional inflow condition at $Re = 50$. Figure 7(f) shows a run using v conditions everywhere. The

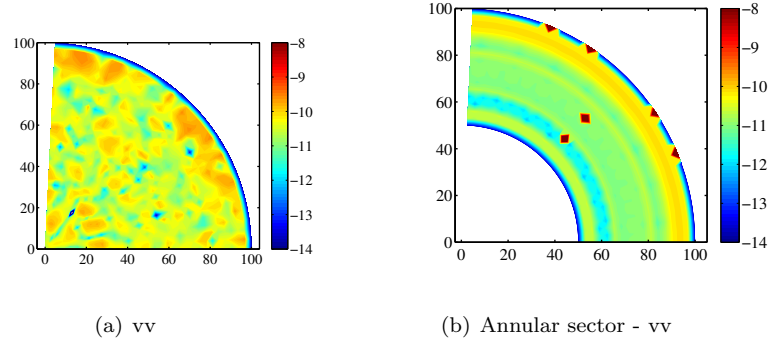


FIGURE 8. Relative error of W averaged in the vertical direction. The axis show the x and y component in the plane. As usual, the first letters denotes the top boundary condition and the last letter the radial boundary condition. The colourbar is shown in \log_{10} scale.

relative error is also of the same order as the error when simulating the whole disk, although, it has a different distribution across the domain.

The amplitude of the relative errors averaged in the vertical direction can be seen in figure 8. Panel (b) shows the annular sector with vv conditions and (a) shows the a quarter of the whole mesh with vv conditions. For both figures, there are larger errors towards higher radius where also the elements are larger. For the annular sector, (b), this structure is seen clearly and it follows an arc as do the elements in the mesh. The annular sector will be further discussed in the next section about grid dependence and resolution, together with figure 7(d) which has not been discussed so far.

7. Grid and resolution dependence of the simulations

Results from both the whole disk mesh and the annular sector mesh have already been shown in the previous section regarding the influence of boundary conditions. In addition, there are differences between the two setups not involving the boundary conditions but concerning the interpolation and the computational efficiency.

When using the annular sector mesh, there are spots of errors seen within the domain, see figure 7(f) and figure 8(b). These errors are due to the interpolation routine since they cannot be found when visualizing the solution directly on the DNS grid (not shown). The order of these errors is 10^{-5} , and they always occur close to an element boundary. The reason for the error was shown to be based within the interpolation algorithm, where sometimes the routine was extrapolating instead of interpolating. These interpolation errors can however be eliminated here by changing the number of elements in the θ

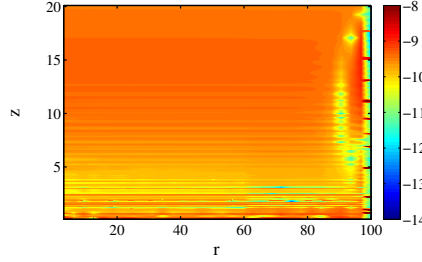


FIGURE 9. Relative error of W . The values are averaged in the azimuthal direction and show a simulation where the height is extended to $z = 20$ using v boundary condition everywhere. The colourbar is shown in \log_{10} scale.

direction from 8 (figure 3(a)) to 9 (not shown). The interpolation routine is thus dependent on the grid used for the specific simulation.

The largest advantage of using the annular sector over the whole disk is however that the number of elements can be reduced considerably, decreasing the number of spectral elements from 3072 to 512. The computational time saved is actually more than that fraction since the CFL number can be decreased from 0.425 to 0.257, making it possible to take larger time steps. However, as seen in figure 7(f) and figure 8(b) there is a resolution dependence with radius showing an error increase, which is not as pronounced for the whole disk as for the annular sector. However, the amplitude of the errors never exceeds the errors of the whole mesh still favouring the annular sector.

To investigate if there is a change of the solution when elevating the resolution, the mesh of figure 3(b) was used. An h -refinement was done where the spectral elements were doubled in the radial and azimuthal direction, and in the vertical direction their number increased to 20 from 16. The stretching factor remained at $s = 1.15$ whereas Δz decreased to 0.1. This led to a total number of spectral elements of 15360. A polynomial order of 8 is still used and the simulation ran for one rotation. However, the time step had to be decreased to keep the CFL number lower than 0.5. The error could be seen to be decreased across the whole domain, compare figure 7(d) and 7(a).

For future simulations, a height of $z = 20$ is desired in Nek5000 and the height of the domain of the whole mesh, figure 3(b), was increased to $z = 20$. The wall-normal resolution was kept the same as in previous simulations close to the wall ($\Delta z = 0.2$) however additional elements were extending the mesh at the top. Also refining the mesh in the r - θ directions the resulting relative error is seen in figure 9. Here v conditions are used. The values are not reaching the same accuracy as in figure 7(a), although this can be achieved by refining the mesh further in the r - θ direction.

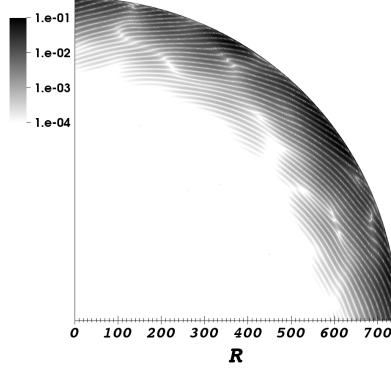


FIGURE 10. A laminar simulation with a mesh stretching from $r = 150$ to 743 . The absolute value of W is shown at $z = 1.3$ where the colourbar is in \log_{10} scale.

8. Going towards higher Reynolds numbers

When higher Reynolds numbers are simulated with Nek5000, the flow is more easily disturbed compared with having an edge at $R = 100$. This is since there are several unstable modes able to grow, both downstream and upstream, see *e.g.* Lingwood (1995). The upstream mode can in particular create problems at the radial outer boundary since the boundary itself can then be a source of disturbances propagating inwards toward the centre of the disk. An example of such a phenomena is shown in figure 10, when laminar flow is simulated with Dirichlet boundary conditions everywhere on an annular sector stretching from radius 150 to 743 . The colour bar is shown in \log_{10} scale and the absolute W -values at a nondimensional height $z = 1.3$ is shown. The disturbances are still growing when this snapshot is taken at a time of π , when the disk has rotated half a revolution. The figure is taken from a simulation when the mesh in the vertical direction had single precision errors. These caused sufficiently large disturbances at the outflow boundary (Dirichlet conditions) and allowed the upstream mode existing at these high Reynolds numbers to bring these disturbances into the domain. When the same simulation was conducted with mesh points in double precision in the vertical direction, no such errors could be seen. For future simulations at similar Reynolds numbers, there will be disturbances induced inside the domain, and a sponge layer will be used to remove the disturbances before reaching the boundary.

9. Summary and Outlook

The laminar von Kármán flow has been set up and simulated in the spectral-element model Nek5000. A numerical solution for the ODE describing the

similarity solution was used to estimate the accuracy of the interpolation routine. The accuracy was found to be of the order 10^{-8} - 10^{-12} for the velocity profiles. This routine was also found to sometimes fail close to element boundaries. The relative errors in these points were in the order 10^{-5} . Since the error occurs in the same position for all time steps during a simulation, it is easy to pinpoint them and find methods to eliminate them, *e.g.* by rearranging the elements. For the annular sector mesh, the errors were found to be eliminated when using a mesh with 9 elements in the azimuthal direction instead of 8. For future simulations, a check for such points should be made. The advantage of using the interpolation routine within Nek5000 is to simplify the post-processing scripts without having to compromise the accuracy of the solution with *e.g.* low-order interpolation.

No dependence on the scaling of the governing equations was shown when running three different cases. For further simulations in Nek5000, the scaling `sc3` will mainly be used since this is consistent with the scaling used in previous work (*e.g.* von Kármán 1921; Lingwood 1995; Imayama *et al.* 2012) where $R = r$. For running simulations in the rotating reference frame compared with the laboratory frame, there was a slight time increase for each time step however an advantage of the rotating frame is the stationary disk, enabling a more straight-forward inclusion of surface roughness into the geometry.

From boundary-condition tests, results showing how the different boundary conditions affect the solution are given concluding that the condition ON or v on top, and v on the outer radial boundary, were found to give the lowest error when compared with the ODE solution, see figure 7(a) and (b). For the other boundary conditions, errors arose close to either the top or the radial boundaries contaminating the domain inward. For future simulations when disturbances are introduced into the domain, using only v in the radial direction would most likely cause reflections. A sponge region can then be combined with this condition. This sponge layer would kill the disturbances before reaching the boundary by using a forcing term, and the flow would then leave the domain through the v condition. This non-reflecting boundary condition has earlier been seen to work well for incompressible stability calculations (Kloker & Konzelmann 1993) and will be further investigated in Nek5000 in combination with new simulations. There is a possibility to implement new boundary conditions for Nek5000 and one option for this would be the advective boundary condition allowing small disturbances to pass out from the domain. This condition can be formulated as $\partial\varphi/\partial t + V\partial\varphi/\partial n = 0$ (Colonus 2004) where Xu & Lin (2007) has specifically implemented this for their spectral-element code. A velocity component is here expressed as φ , V is the outlet convection velocity to be set, and n is the normal to the outflow boundary. The outlet convection velocity must be as close as possible to the actual local phase velocity of the wave packets, which can be either obtained from linear theory (in case of

low-amplitude disturbances) or from temporal averaging in the case of turbulent outflow. This boundary condition would eliminate the usage of a sponge. A version of this boundary condition has been applied by Viaud *et al.* (2008, 2011) when simulating an open rotating cavity. Similar wave-like boundary conditions have also been applied for the rotating-disk case in a linear code (Davies & Carpenter 2001, 2003).

Going back to the laminar flow simulations, the boundary conditions set for the top boundary provide information about the similarity solution from the ODE solver. However, what must be mentioned in this context is that the ON_0 condition essentially contains the same boundary condition information set at the top of the ODE-solver domain. Since this solver uses a domain up to $z = 20$, the ON and ON_0 condition are set exactly equal if the height of the Nek5000 domain is $z = 20$. The ON_0 boundary condition would be particularly useful for future simulations when the laminar flow is changed to a transitional and/or turbulent one. The simulation domain would then be higher than $z = 20$ due to a thicker boundary layer, and the von Kármán similarity solution would be allowed to change and the boundary layer can develop in its own nature.

For further simulations including higher Reynolds numbers, the mesh will also have to be refined to resolve the disturbances put into the flow. For the grid structure, the annular sector had a large advantage in the low computational costs and therefore it will mainly be used, with the condition that it should also be checked for interpolation errors. Note, however, that when dividing the domain in the azimuthal direction, there is a limitation on the possible wavenumbers in this same direction.

The general conclusions from this report is that the von Kármán flow can be simulated in Nek5000. The method was robust when it came to using different scaling and reference frames. It was also possible to anticipate how the different boundary conditions would behave showing a promising outlook for the future.

This work is supported by the Swedish Research Council through the ASTRID project and the Linné FLOW Centre.

Bibliography

- COLONIUS, T. 2004 Modeling artificial boundary conditions for compressible flow. *Annu. Rev. Fluid Mech.* **36**.
- DAVIES, C. & CARPENTER, P. W. 2001 A novel velocity–vorticity formulation of the Navier–Stokes equations with applications to boundary layer disturbance evolution. *J. Comput. Phys.* **172**, 119–165.
- DAVIES, C. & CARPENTER, P. W. 2003 Global behaviour corresponding to the absolute instability of the rotating-disc boundary layer. *J. Fluid Mech.* **486**, 287–329.
- DEVILLE, M. O., FISCHER, P. F. & MUND, E. H. 2002 *High-Order Methods for Incompressible Fluid Flow*. Cambridge University Press.
- FISCHER, P. F., LOTTES, J. W. & KERKEMEIER, S. G. 2012 Nek5000. *Web page*. <http://nek5000.mcs.anl.gov>.
- IMAYAMA, S., ALFREDSSON, P. H. & LINGWOOD, R. J. 2012 A new way to describe the transition characteristics of a rotating-disk boundary-layer flow. *Phys. Fluids* **24**, 031701.
- VON KÁRMÁN, T. 1921 Über laminare und turbulente Reibung. *Z. Angew. Math. Mech.* **1**, 232–252.
- KARNIADAKIS, G. E., ISRAELI, M. & ORSZAG, S. A. 1991 High-order splitting methods for the incompressible Navier-Stokes equations. *J. Comput. Phys.* **97**, 414–443.
- KLOKER, M. & KONZELMANN, U. 1993 Outflow boundary conditions for spatial Navier-Stokes simulations of transition boundary layers. *AIAA J.* **31**, 620–628.
- LINGWOOD, R. J. 1995 Absolute instability of the boundary layer on a rotating disk. *J. Fluid Mech.* **299**, 17–33.
- LINGWOOD, R. J. 1997 Absolute instability of the Ekman layer and related rotating flows. *J. Fluid Mech.* **331**, 405–428.
- VIAUD, B., SERRE, E. & CHOMAZ, J.-M. 2008 The elephant mode between two rotating disks. *J. Fluid Mech.* **598**, 451–464.
- VIAUD, B., SERRE, E. & CHOMAZ, J.-M. 2011 Transition to turbulence through steep global-modes cascade in an open rotating cavity. *J. Fluid Mech.* **688**, 493–506.
- XU, C. & LIN, Y. 2007 A numerical comparison of outflow boundary conditions for spectral element simulations of incompressible flows. *Commun. Comput. Phys.* **2**, 477–500.